

6 Muon System

In this chapter the Muon System is described. The first section is devoted to the changes in the muon spectrometer chamber layout since the muon TDR [6-1]. The geometrical acceptance and the single muon performance are discussed in the two subsequent sections.

6.1 Muon spectrometer layout

The layout of the muon spectrometer has been described in detail in the muon TDR [6-1], based on layout version L. The Muon System simulation described here uses layout version M2, the design as of February 1998. The only significant difference between these layouts concerns the chambers in the middle and outer end-cap stations. All other modifications are small adjustments which either slightly improve the acceptance and performance or result in minor losses due to unavoidable constraints from other parts of the detector. These changes are described below in detail.

The layout described here is likely to be close to the final layout except for regions where services (mainly of the Inner Detector and of the calorimeter) will be routed through the Muon System. This affects mostly the regions around $\eta = 0$ and some of the inner end-cap chambers.

6.1.1 The rearrangement of the end-cap chambers

Following the revision of the overall ATLAS access strategy (see Chapter 14 in Ref. [6-2]), the layout of the middle and outer stations of the end-cap chambers has been modified. The new access scheme allows for a simpler arrangement of the EM and EO chambers since no separation between inner and outer chamber rings is required and all chambers (MDTs and TGCs) within a station can be located in the same plane. With the new layout of the forward region there is no need for holes in the muon chambers for the passage of the detector rails, a major simplification for the construction of the muon chambers and a net gain in acceptance.

A longitudinal view of the new chamber arrangement is shown in Figure 6-1. All end-cap chambers are now separated by 20 mm (instead of 15 mm) radially from their neighbours. This follows the same scheme as applied in the barrel. The influence on acceptance should be minor since there is still full coverage in the transition between two chambers.

In changing the layout of the end-cap chambers, the chamber naming scheme was changed with respect to muon TDR Chapter 3. All chambers are now called E(nd-cap) chambers and the numbering of the chambers inside each plane is unique, running from 1 to n with increasing radius. Thus the names are EMS and EML for the MDT chambers and TM1, TM2, TM3 for the TGCs in the three trigger planes.

6.1.1.1 EM chambers

The layout of the MDTs in the middle station is shown in Figures 6-2 and 6-3. All chambers within a plane are mounted on a common support structure the form of a wheel suspended from two rails connected at a height of about 19 m to the cavern walls [6-3]. On each side of the

detector there are four such support wheels, one for the MDTs and three for the three TGC planes. As before, the MDTs are arranged in small and large chambers; now, however, there is no radial gap between EMx.2 and EMx.3.

The TGC layout is shown in Figures 6-4 and 6-5. It has been considerably simplified by the placing of all chambers of a trigger plane on the same structure. The acceptance of the TGC system remains unchanged, with the exception of a small improvement due to avoidance of an overlap between the movable and fixed chambers of the TDR layout. The layout of the TGCs on the three wheels is shown for the example of the TGC1 plane in Figure 6-4. The layouts of the TGC2 and TGC3 planes follow the same general scheme with the whole structure at higher radius. The outer dimensions of the three TGC planes are indicated in Figure 6-1.

6.1.1.2 EO chambers

Like the EM chambers, the EO chambers have also been arranged in a single plane. The inner ring of chambers (as in the TDR layout) has been moved about 1.1 m closer to the interaction point (IP) and the outer ring moved about 0.5 m away from the IP. The new positions in z are 21 332 mm for the EOL and 21 746 mm for the EOS chambers. In addition, all chambers have the same spacer thickness of 170 mm. The internal layout of the chambers is shown in Figure 6-3. The chambers are mounted on the end-wall scaffolding structure.

6.1.2 The crack region

In the region around $\eta = 0$ a gap of 300 mm in the BIL, BML, BMS, and BOL chambers had been foreseen for the passage of the services of the Inner Detector, the solenoid, and the calorimeters. The exact space requirements for these services are not yet defined and have not been taken into account yet. It is clear that, at least in some sectors, the foreseen space is not sufficient and needs to be increased. Estimates of the required space are difficult to make at this time. It is likely that different openings will be required for each sector. It is hoped that on average the opening will not increase by more than a factor two.

6.1.3 Other changes and changes after version M2

The other main change of the layout is the reduction of the longitudinal gaps between the BMS chambers as the result of decreasing the longitudinal extent of the barrel toroid ribs from 300 mm to 240 mm. This leads to some improved coverage in the barrel, in particular for the trigger.

Changes to the layout since version M2 are small (excluding the necessary future changes with respect to the passage of services). They concern some internal rearrangement of chambers which should have no impact on the acceptance calculations, and some small adjustments in chamber positions in order to avoid interference with other detector parts.

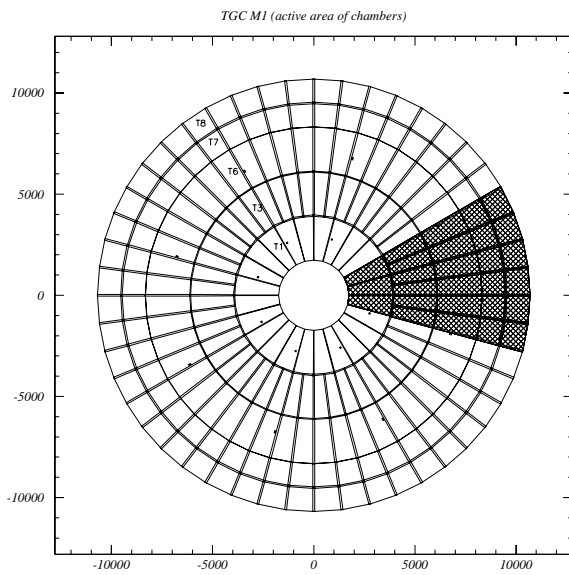


Figure 6-4 Layout of TGCs in the TM1 plane.

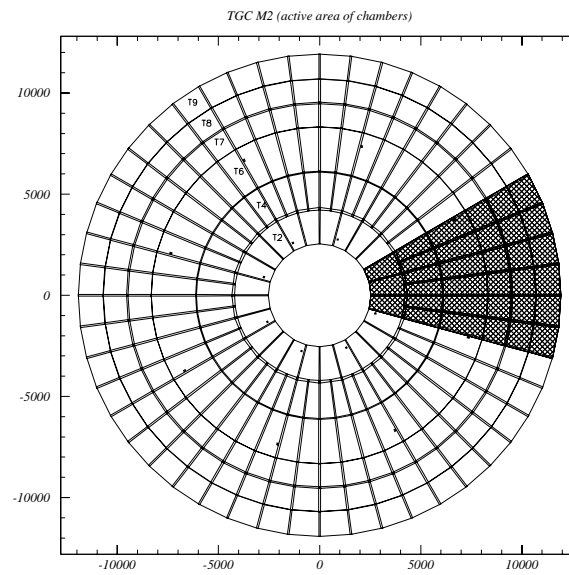


Figure 6-5 Layout of TGCs in the TM2 and TM3 plane; shown is here the TGC2 wheel; the TGC3 chamber layout is almost identical.

6.2 Geometrical acceptance

6.2.1 Monte Carlo simulation

In the Monte Carlo simulation used for acceptance studies, particular care has been taken in describing the different technologies of the Muon System: MDTs, CSCs, RPCs and TGCs are all simulated in detail from the geometrical point of view but are all treated as generic detectors decomposing the physical volume of each chamber into sensitive and non sensitive regions. Different layers of sensitive regions are interleaved with layers of passive material following in detail the layout of the Muon System. In the simulation of the various subdetectors one layer of tubes, or of strips or wires is defined as a sensitive plane.

Unless otherwise stated, all results presented in this section refer to infinite-momentum muons generated at the nominal pp interaction point with no interaction with matter. Detector hits are recorded for each individual sensitive element traversed by the particle. Additional studies, which are not reported here, were carried out to study the acceptance of the apparatus for low momentum particles, while Higgs studies (from the acceptance point of view) are reported in a subsequent subsection.

This simulation also includes the finite length of the interaction region, the electromagnetic and hadronic calorimeters, the magnet structures, and the magnetic fields, in order to correctly account for magnetic bending, multiple scattering, and all energy loss processes when necessary.

6.2.2 Precision chambers

The precision chamber acceptance is computed on the basis of so-called 'superpoints'. A superpoint is a coincidence of at least six hits in six different sensitive planes in one chamber. Such a hit multiplicity requirement fully exploits the tracking resolution in most chambers, and ensures local vector measurement capability. A 'half-superpoint' is a coincidence of at least three hits in the adjacent layers that form a multi-layer; it allows for momentum measurement, albeit with slightly degraded resolution.

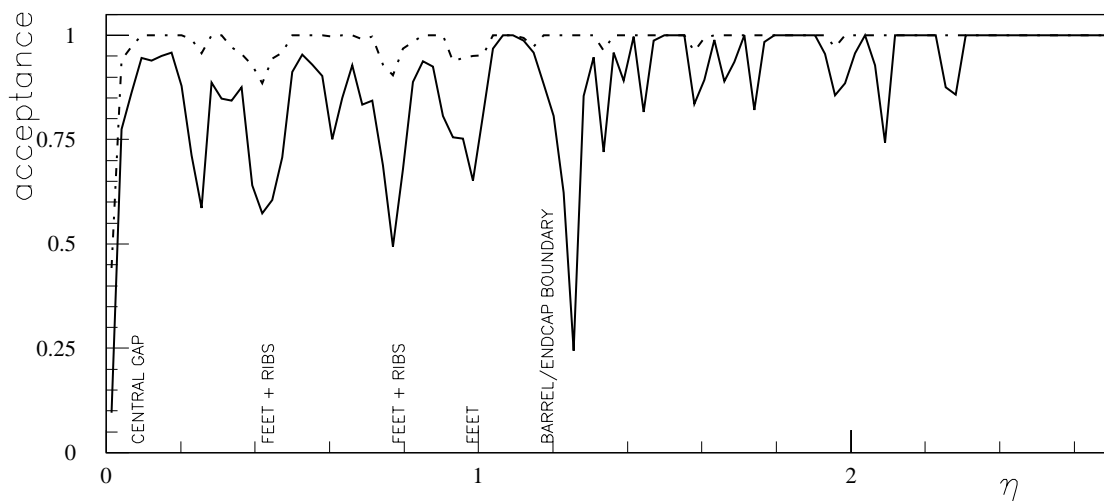


Figure 6-6 Acceptance for the requirements of one superpoint (dash-dotted line) and three superpoints (solid line) in the three stations of the precision chamber system, as a function of pseudorapidity and averaged over azimuthal angle. The acceptance for a coincidence of two superpoints is nearly indistinguishable from that for one superpoint, and is not shown in the figure.

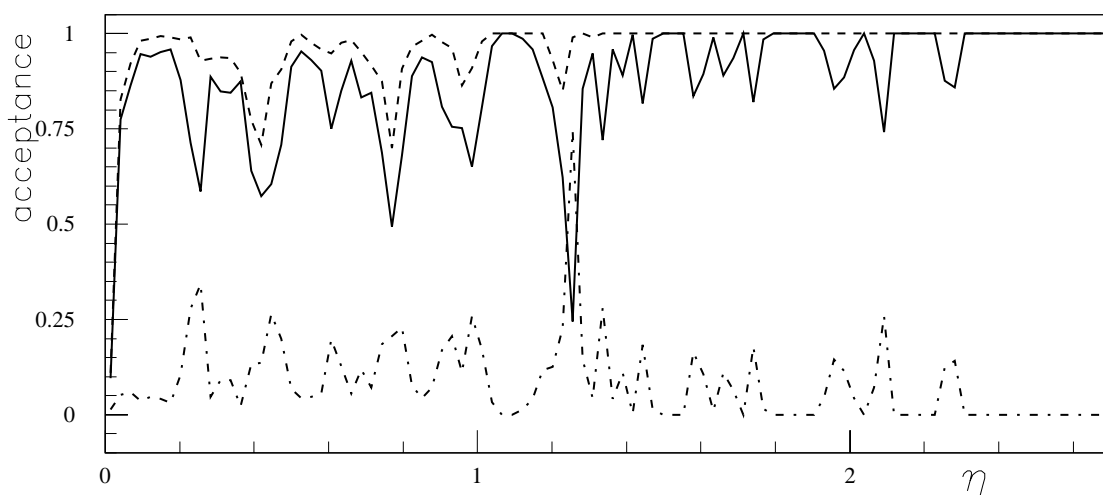


Figure 6-7 Comparison of acceptance for three superpoints (solid line) and three half-superpoints (dashed line) in the precision chamber system, as a function of pseudorapidity and averaged over azimuthal angle. The dash-dotted line shows the difference between the two categories.

Acceptance for different combinations of superpoint requirements, averaged over azimuth, are shown in Figures 6-6 and 6-7. Figure 6-6 compares the acceptance for three superpoints, providing optimal track and momentum reconstruction, to the acceptance for one superpoint, which provides limited muon identification at low occupancy levels. Acceptance losses due to the mechanical structures of the barrel magnet, in the intermediate region between barrel and end-cap or generated by cracks between adjacent rings of end-cap chambers, are visible for tight multiplicity requirements.

Figure 6-7 shows the acceptance for three superpoints in comparison to the acceptance for three half-superpoints as a function of η averaged over the azimuthal angle. The average acceptance increases from ~ 0.90 to ~ 0.96 on relaxing the multiplicity requirement from three to three-half superpoints.

Figure 6-8 shows the acceptance for three superpoints as a function of azimuth, integrated over $|\eta| < 2.7$. In this view, acceptance losses are mostly due to the magnet feet centred at 247.5° and 292.5° . The eightfold detector modularity is clearly seen from the acceptance loss near the sector boundaries. Precision chamber acceptance for the different categories, averaged over η and ϕ , are shown in Table 6-1.

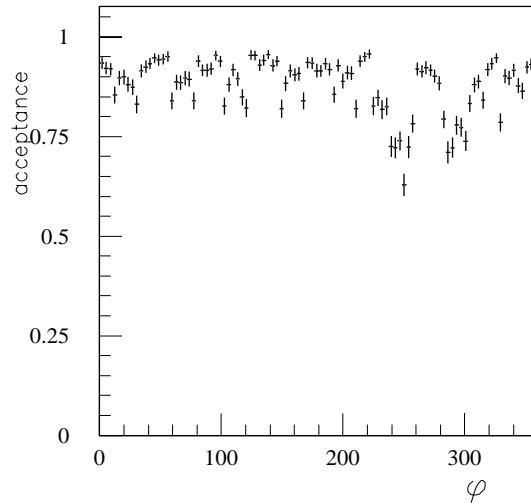


Figure 6-8 Precision chamber acceptance as a function of azimuthal angle, requiring three superpoints, averaged over pseudorapidity.

Table 6-1 Geometrical acceptance of the precision chamber system (averaged over $|\eta| < 2.7$), for different coincidence requirements discussed in the text. The precision chamber acceptance is averaged over $0^\circ < \phi < 360^\circ$.

Precision chamber acceptance category	Average acceptance
1 superpoint	0.997
2 half-superpoints	0.994
2 superpoints	0.989
3 half-superpoints	0.961
3 superpoints	0.896

6.2.3 Trigger chambers

The trigger system in ATLAS is composed of the RPCs ($|\eta| < 1.05$) and the TGCs ($1.05 < |\eta| < 2.4$). The trigger chamber acceptance has been evaluated and discussed in the LVL1 Trigger TDR [6-4] and in the Trigger Performance Report [6-5].

In the RPC system, a low p_T coincidence is defined by those tracks that have hits in at least three of the four inner trigger planes. A high p_T coincidence is the logical ‘AND’ of a low p_T coincidence and at least one hit in the two planes of the outer stations. A similar algorithm is used in the case of the TGCs [6-4]. Here a low p_T coincidence is a combination of three out of four hits in the outer trigger station (two doublet chambers); a high p_T coincidence is the ‘AND’ of a low p_T coincidence and at least two hits in the three planes in the inner trigger station (triplet chambers).

The geometrical acceptance is shown in Table 6-2 for the barrel and end-cap independently and for the combined system. Acceptance loss in the range $0 < |\eta| < 2.4$ averaged over full azimuth is ~ 0.06 and ~ 0.065 for the low p_T and high p_T coincidences, respectively. No windowing effect in the LVL1 muon trigger and no contributions from the alignment corridors are considered in this study.

Table 6-2 Average acceptance for the trigger chambers system.

Trigger chambers	Barrel	End-cap	Combined system
low p_T coincidence	0.91	0.98	0.94
high p_T coincidence	0.88	0.97	0.93

6.2.4 Acceptance study of $H \rightarrow ZZ^* \rightarrow \mu\mu\mu\mu$

The Higgs boson decay to four muons is a benchmark process for muon detectors at the LHC. In order to evaluate in detail the effects of the muon trigger system acceptance on the Higgs detection capabilities, a sample of Standard Model Higgs decays to four muons through the process $H \rightarrow ZZ^* \rightarrow \mu\mu\mu\mu$ was investigated.

Samples of Higgs events in the mass range 120–180 GeV have been studied in order to evaluate the geometrical acceptance of the precision chamber system and of the trigger system for multi-muon event detection. The acceptance of the trigger system, normalised to the precision chamber acceptance, for two muons is very close to 1, for three muons is about 0.96 and for four muons is about 0.69, independent of the Higgs mass. Details of this analysis can be found in [6-4].

6.3 Single muon performance

6.3.1 Pattern recognition and reconstruction

Compared to most spectrometers in high energy physics experiments to date, the ATLAS muon spectrometer is unique in several aspects. It was designed to maintain high performance, in terms of detection efficiency, momentum resolution and fake track rejection, in the difficult LHC

environment within a ‘reasonable’ cost. One of the drawbacks of this performance against cost compromise is that many features of this spectrometer make the pattern recognition and track reconstruction more challenging.

- The ‘open’ air-core toroid concept leads to a magnetic field which, in addition to being relatively modest in magnitude (0.5 T in average), is very inhomogeneous, so that particle trajectories can be very peculiar (especially at low p_T) and cannot be approximated by simple analytical descriptions.
- The unusually large size of the system (22 m in diameter, 44 m in length) implies large distances between measuring stations which induce significant extrapolation uncertainties.
- Due to the cost constraint limiting the number of detector channels, redundancy is small and the precision chambers measure only one coordinate (approximately the bending direction). Thus, no precise three dimensional information is available and the accuracy in the so-called ‘second coordinate’ is two orders of magnitude worse (1 cm with respect to 80 μm) than in the principal coordinate accuracy.
- Furthermore, the high background level in the experimental hall enhances most of the problems mentioned above.

These features of the muon spectrometer not only put severe constraints on the software that will exploit its data, but also on its hardware.

- In addition to the sophisticated optical system that will ensure, by means of software corrections, a precision of 30 μm on the alignment of the precision chambers, it is also necessary to be able to mechanically position all these chambers such that, in each octant, their wires are parallel within one (or at most a few) milliradian(s). In absence of such precise alignment the inaccuracy of the second coordinate degrades the first coordinate accuracy.
- The magnetic field reconstruction algorithms have been tested with Monte-Carlo simulation and, recently, on a small test superconducting ‘race-track’ coil [6-6]. They can provide the intended accuracy (roughly 3 Tm) if and only if unforeseen magnetic masses are completely avoided inside the toroidal magnets and anywhere in its vicinity.

The basic principles and main steps of the pattern recognition software have been described in muon TDR [6-1]. Since that time, a large number of technical improvements have been introduced to this software essentially to improve the reconstruction efficiency at low p_T while keeping the CPU usage at an acceptable level.

To improve the low p_T efficiency without introducing too many fake tracks, it is crucial to take into account as precisely as possible the effects of multiple scattering of muons in the material of the spectrometer. Indeed, in spite of the air-core toroids, the amount of material traversed by a muon in the spectrometer can be relatively large and very unevenly distributed along its trajectory. That is why a very detailed description of the passive material of the Muon System (as well as of the whole experiment) has been introduced, together with the geometry of the active detectors, into the pattern recognition and reconstruction software. This information is retrieved from a muon database [6-7] where the geometry and composition of the ATLAS detector materials are described. As an example of the level of detail of the material considered in the reconstruction software, the Figure 6-i displays a muon track traversing the spectrometer.

6.3.2 Tracking back to the beam and energy loss in the calorimeters

An additional improvement in the reconstruction, made possible by the accurate material description, deals with energy losses in the calorimeters as well as in the Muon System itself. Although energy losses and their distribution along the muon track have a very small impact on muon reconstruction inside the Muon System, they play an important role in tracking back the reconstructed muon to the beam line. During this ‘backtracking’, the muon momentum can be corrected for using the energy measured in the calorimeter cells it has traversed. This procedure, however, is potentially dangerous and it is justified only for isolated high p_T muons (which have a higher probability of ‘catastrophic’ energy loss). In most cases, it is safer to correct the muon momentum only for the mean energy loss, estimated from the reconstructed momentum as well as from the amount and the nature of the material traversed by the reconstructed trajectory. This estimated mean energy loss correction is shown in Figure 6-9 as a function of η , for two extreme values of p_T (5 and 500 GeV), and compared to the average ‘true’ energy loss as simulated event-by-event with GEANT.

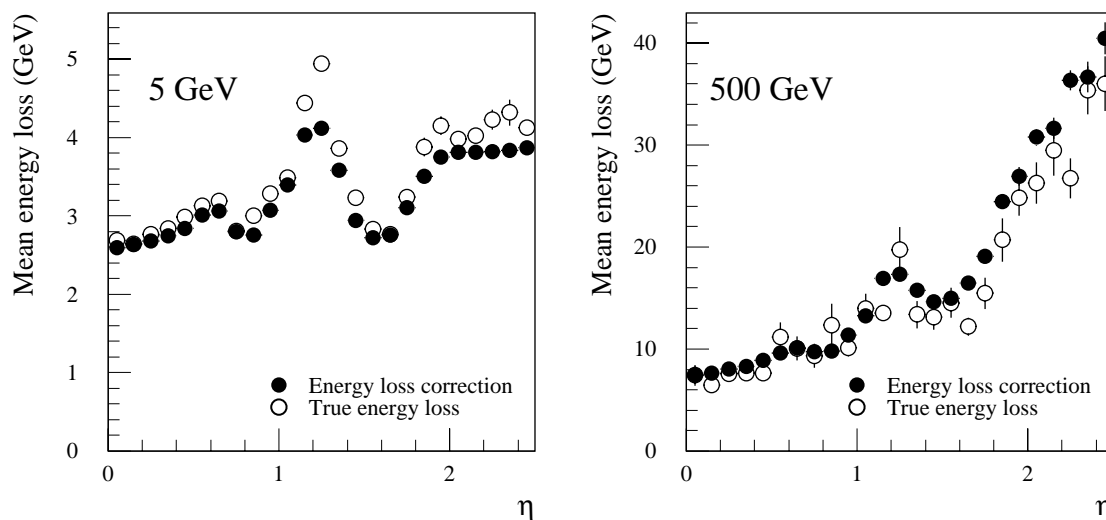


Figure 6-9 Mean energy loss versus η for muons of $p_T = 5$ GeV (left) and 500 GeV (right). The open circles represent the actual ‘true’ mean energy loss, as obtained from a GEANT simulation, whereas the filled circles represent the estimated mean energy loss as obtained from the detailed representation of the calorimeters material in the reconstruction program.

Figure 6-9 shows that the reconstruction program is able to predict with good accuracy the energy loss over a wide range of muon momenta. The remaining small discrepancies between the GEANT simulation and the estimated energy loss will be further studied. Since the agreement is satisfactory, however, the backtracking procedure has been included in the muon reconstruction software in addition to methods to compute and to transport the full covariance matrix associated with each reconstructed track. Reconstructed track parameters with their full covariance matrices are provided at three locations:

1. At the entrance to the muon spectrometer, *i.e.* on the cylinder $|z| = 682$ cm, $R = 425$ cm.
2. At the entrance to the calorimeters, *i.e.* on the cylinder $|z| = 320$ cm, $R = 105$ cm.
3. At the perigee of the track.

To illustrate the consistency of these covariance matrices, distributions of the pull of the inverse of the transverse momentum at the perigee of the reconstructed tracks are plotted in Figure 6-10 for four different fixed p_T single muon samples. The pull is defined here as the difference be-

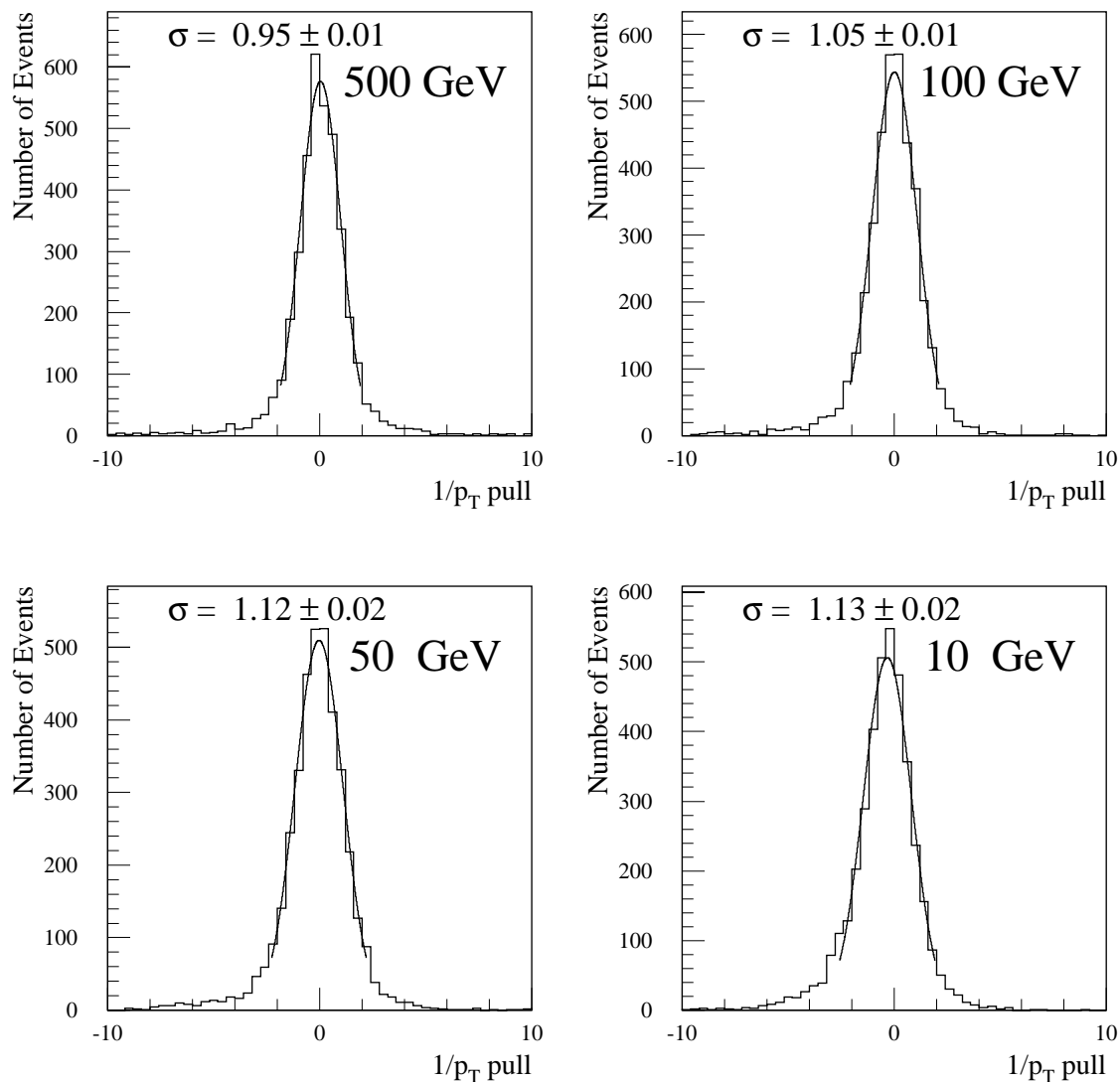


Figure 6-10 Distribution of the pull of the inverse transverse momentum of the muon spectrometer reconstructed tracks propagated down to the vertex.

tween the reconstructed and the true values normalised to the error on the reconstructed value. In spite of a very inhomogeneous momentum resolution (see next paragraph), the fact that these distributions remain roughly compatible with Gaussians of unit width for muons of p_T from 10 GeV up to 500 GeV illustrates the consistency of these covariance matrices.

6.3.3 Momentum resolution

The semi-analytical evaluation of the muon momentum resolution (see Section 12.3.2 of [6-1]) has also benefited from the above mentioned refinements in the material description. The new version of this software performs full 3D tracking for each given set of (p_T, η, ϕ) and takes into account all the traversed material whereas earlier versions used only the integrated magnetic deflection along a straight line and a simplified parametrised description of the material. Compared to resolution figures obtained in the muon TDR [6-1], the structure of the various spikes in the (η, ϕ) plane at moderate p_T is more detailed and leads to a degradation of the average resolution. However this small worsening of the resolution is compensated by two other effects:

1. The holes that were foreseen in the EM plane of muon chamber (to allow for the rails supporting the calorimeters and Inner Detector) have disappeared (the rails are now presumed to be dismantled after installation – see Section 6.1.1). This has cured the strong degradation of the ϕ -averaged resolution that resulted from the absence of measurement inside these holes (around $\eta = 1.6$).
2. The value assumed, in the computation of the expected momentum resolution, for the averaged spatial resolution of an MDT multi-layer as well as the value of the averaged global misalignment of the multi-layers were somewhat pessimistic. A more realistic re-evaluation of these quantities (*i.e.* assuming 85 μm averaged resolution for each tube and 35 μm misalignment error on the sagitta) leads to a slightly better expected momentum resolution in those (p_T, η, ϕ) regions which are not dominated by multiple scattering effects.

6.3.3.1 Standalone muon momentum resolution

As a first check of this analytical evaluation of the muon momentum resolution, results of the full simulation at various p_T values are compared in Figure 6-11 to the results of a model in which the momenta are smeared according to the analytically computed single muon momentum resolution. In order not to blur the result of the resolution evaluation, this comparison is made for the muon momentum at the entrance to the muon spectrometer so that the fluctuations of energy loss in the calorimeters do not contribute to the resolutions. The agreement is reasonable particularly since the resolution is highly inhomogeneous in the (η, ϕ) plane. In this particular study, chamber misalignment was neglected both for calculated and simulated results.

These results have proved to be independent of the details of the digitisation scheme assumed in the full simulation, as long as the mean spatial resolution of a single tube is not changed. A realistic MDT response simulation including all the effects discussed in Section 6.3.4 yields the same momentum resolution as the simplified digitisation model described in the

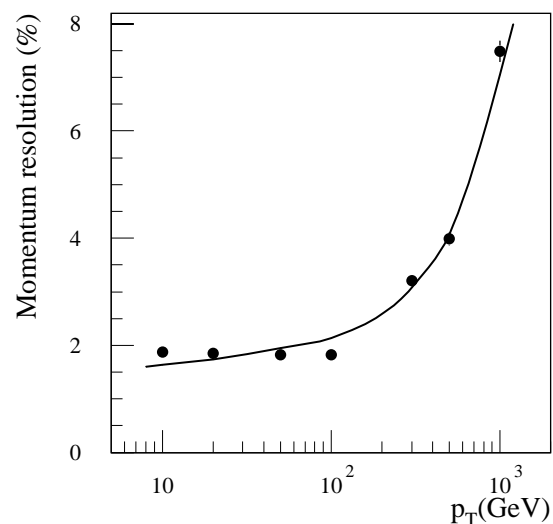


Figure 6-11 Simulated (points) and calculated (line) p_T dependence of the muon momentum resolution, ignoring energy loss fluctuations and for $|\eta| < 1.5$.

muon TDR. It was also found that the presence of non-Gaussian tails in the tube resolution function does not have any impact. This demonstrates the robustness of the reconstruction algorithm against a few hits with large departures from the track.

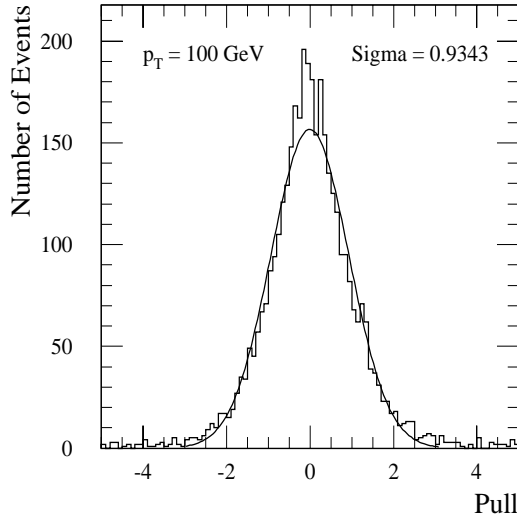


Figure 6-12 Distribution of the momentum pull for $p_T = 100$ GeV.

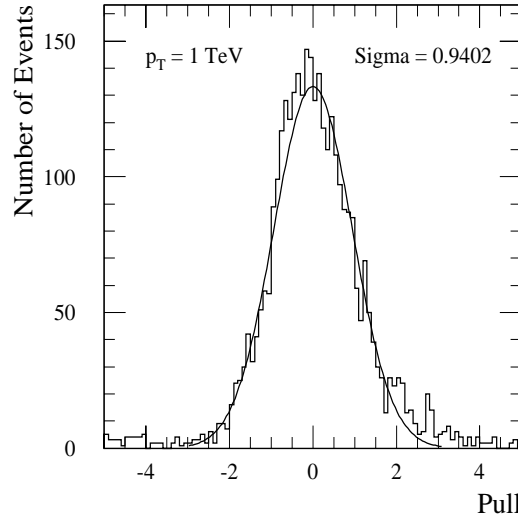


Figure 6-13 Distribution of the momentum pull for $p_T = 1$ TeV.

The agreement between the full simulation and the analytical calculation is best reflected by the distribution of the pulls. If the theoretical prediction σ_{th} is correct for every track, *i.e.* the measured $\Delta p/p$ follows to a Gaussian distribution with standard deviation σ_{th} , the pull will be distributed according to a normal distribution. Figures 6-12 and 6-13 show example distributions for $p_T = 100$ GeV and $p_T = 1$ TeV.

6.3.3.2 Momentum resolution as a function of η and ϕ

The ϕ averaged resolution as a function of η is shown in Figures 6-14 and 6-15 for two values of p_T . In these results, all effects such as chamber misalignment or energy loss fluctuations in the calorimeters are considered. The expected resolutions are slightly better than those quoted in the muon TDR [6-1] for the reasons explained in Section 6.3.3.

The momentum resolution as a function of both η and ϕ is shown in Figure 6-16 for $p_T = 100$ GeV. Compared to the similar figure in the muon TDR [6-1], the wall-like structure near $\eta = 0$ (corresponding to a region of no measurement due to the gap in the muon chambers) has essentially disappeared. This is explained by the fact that, in this new result, the actual curvature of the tracks is taken into account so that most of the tracks hit at least two stations which is sufficient for a (crude) momentum measurement. However it is already foreseen that the gap in the large chambers near $\eta = 0$ will be increased in order to provide enough space for the passage of services (see Section 6.1.2). Compared to the results presented here, a non-negligible loss of acceptance in the $\eta = 0$ region is then to be expected. The small degradation of the resolution that can be seen in Figure 6-16 in the region $1.7 < \eta < 2.2$ and $20^\circ < \phi < 25^\circ$ and that was not present in the corresponding figure of the muon TDR, is due to the material of the 'stay tube' that connects the two flanges of the cryostat of the end cap toroid magnets. The additional mate-

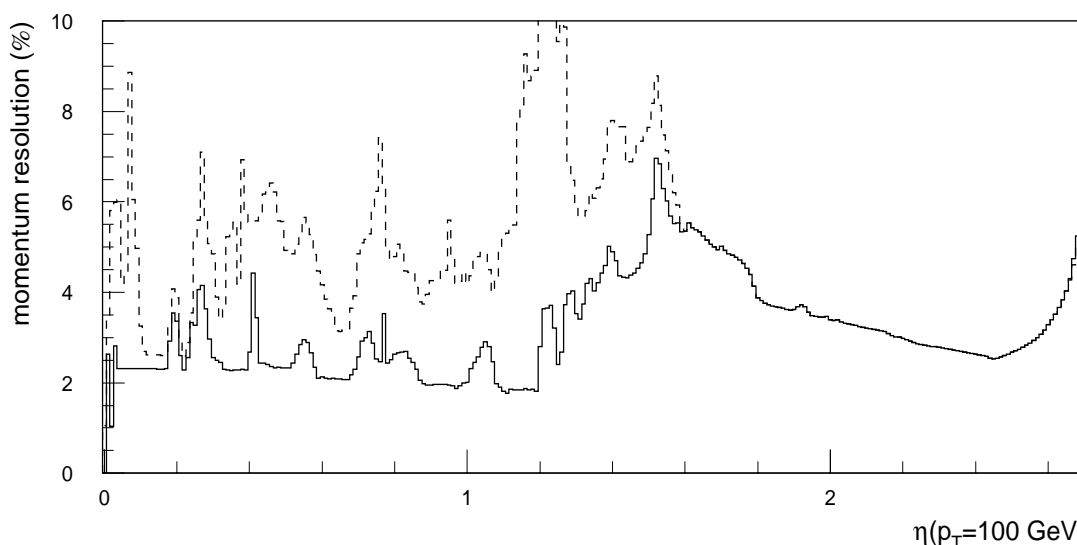


Figure 6-14 Momentum resolution for $p_T = 100 \text{ GeV}$, averaged over ϕ in one octant, as a function of the pseudorapidity. The dashed curve corresponds to the two octants that contain the feet.

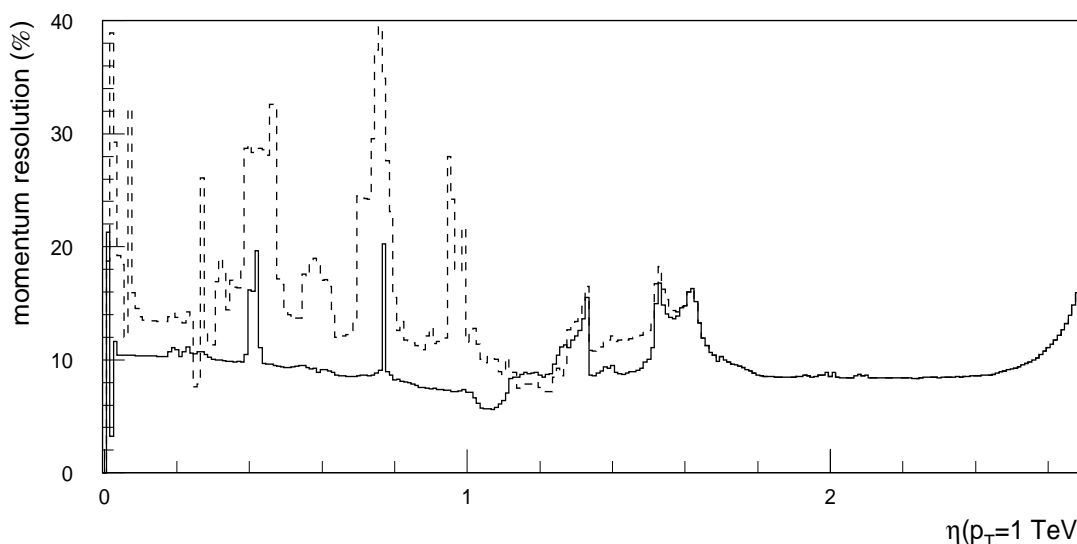


Figure 6-15 As Figure 6-14, for $p_T = 1 \text{ TeV}$.

rial traversed by a muon due to this tube is moderate but the averaged location of this matter being just in the middle of the bending of the muon, it has a non-negligible impact on the momentum resolution.

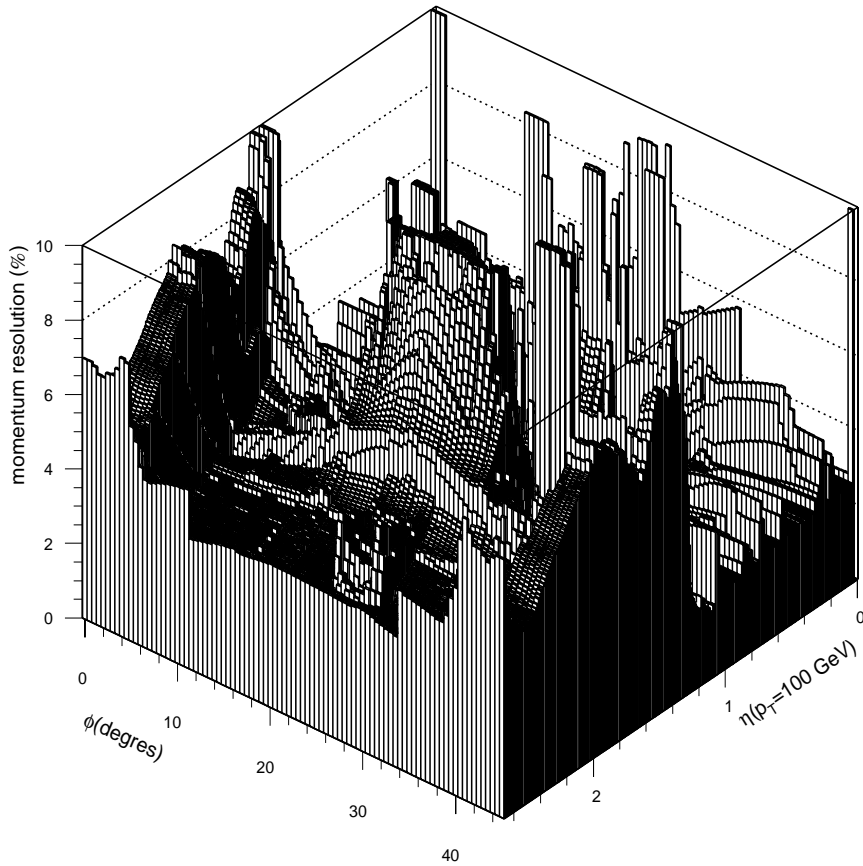


Figure 6-16 Momentum resolution for $p_T = 100$ GeV as a function of η and ϕ .

6.3.3.3 Acceptance versus momentum resolution

A concise way to visualise the performance of the muon spectrometer is to plot, for fixed values of p_T , the fraction of the phase space ($|\eta| < 2.7$) over which the momentum resolution is better than a given value as a function of this value. The momentum resolution results discussed above are presented in such a way in Figure 6-17. Compared to similar plots presented in the muon TDR [6-1], the curves are 'sharper' which means that the resolution is somewhat more homogeneous in the (η, ϕ) phase space. This improvement, which comes mainly from the disappearance of the hole in the EM stations (see above), is welcome because the homogeneity of the resolution may be more important than having a very good resolution in a limited region of the phase space; in a multi-muon event the resolution on the reconstructed mass is dominated by the

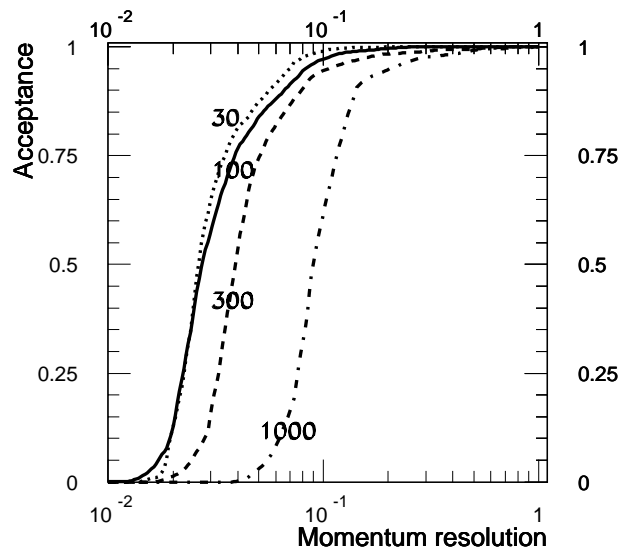


Figure 6-17 Acceptance as a function of momentum resolution for various p_T (see text).

most poorly measured muon. This figure also illustrates the fact that the momentum resolution of the muon spectrometer is better than 5% over 80% of the phase space for a wide range of p_T (roughly from 10 to 300 GeV).

6.3.4 MDT digitisation simulation and impact on reconstruction

First test beams results have allowed the refining of the MDT digitisation simulation relative to that used in the ATLAS muon TDR [6-1]. The impact of this more realistic digitisation on reconstruction efficiency and momentum resolution has been investigated.

For each hit in a drift tube the track radius is converted into a drift time using the $r-t$ relationship and smeared according to the time resolution of a single drift tube. For the muon TDR [6-1] a linear $r-t$ relationship with a maximum drift time of 500 ns and an r -dependent Gaussian resolution with an average of 80 μm (Figure 6-18) were used, which approximates the properties of the gas mixture Ar (91)/N₂ (4)/CH₄ (5). In order to achieve a more realistic description of the MDT response the following effects were added:

- Instead of a linear approximation, the correct $r-t$ relationship of the gas Ar (91)/N₂ (4)/CH₄ (5) as measured in a test beam was introduced into the simulation (see Figure 6-19).
- The spatial resolution was changed to that described by the exact time distributions which significantly deviate from the Gaussian shape at drift distances smaller than 2 mm (Figure 6-20)[6-8].
- The description of the Lorentz effect was improved. For the muon TDR a constant deviation angle for the drifting electrons was assumed. In reality, however, this angle depends on the electric field which is inversely proportional to the distance from the wire. Therefore the new parametrisation of this effect which was extracted from the results of test-beam measurements (Figure 6-21) [6-9], differs considerably from the old model.

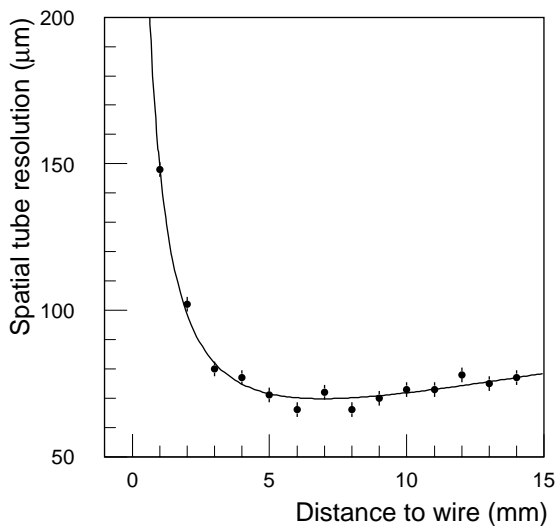


Figure 6-18 Spatial resolution of a single drift tube as a function of the track distance from the wire.

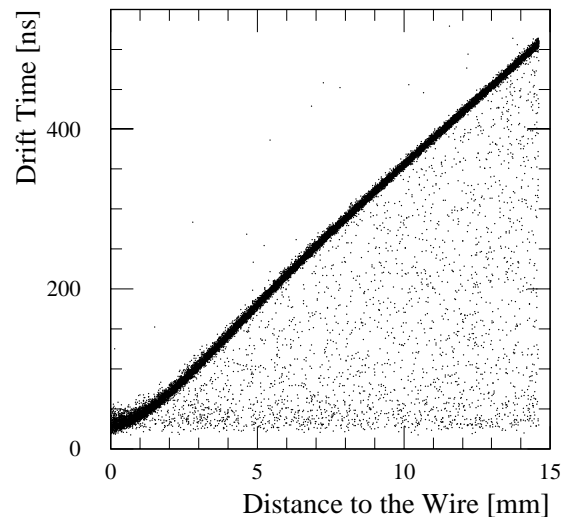


Figure 6-19 $r-t$ relationship for the gas mixture Ar (91)/N₂ (4)/CH₄ (5). The background below the main band is due to Delta rays.

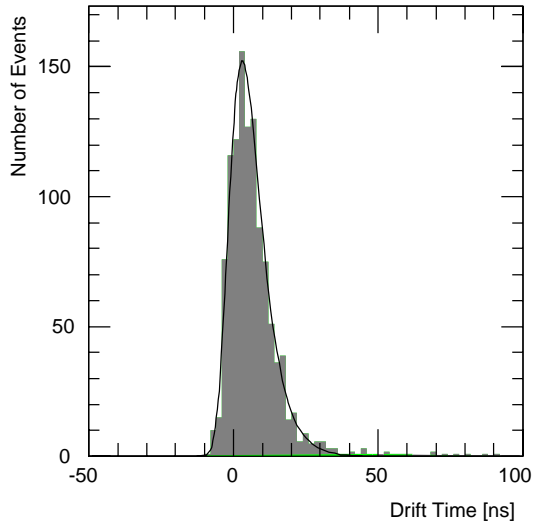


Figure 6-20 Non-Gaussian drift time distribution for $0.25 \text{ mm} < r < 0.3 \text{ mm}$.

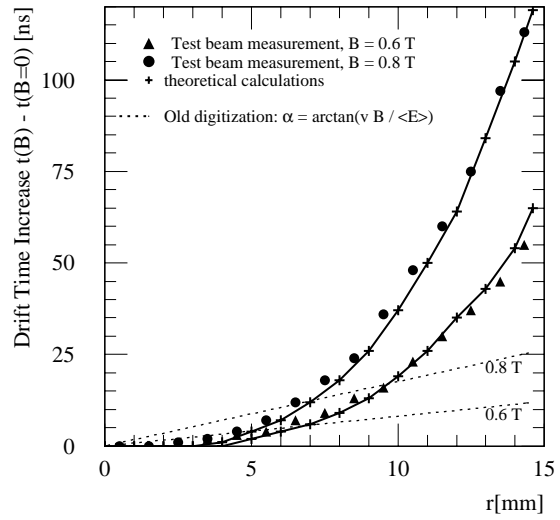


Figure 6-21 Drift time increase due to the Lorentz effect for $B = 0.6 \text{ T}$ and 0.8 T . The points on the solid curve represent a numerical solution of the equations of motion.

In the reconstruction, the same r - t relationship and resolution as used for the digitisation were employed. Only the non-Gaussian tails in the tube resolution function (see Figure 6-20) cannot be taken into account by a reconstruction algorithm based on χ^2 minimisation. Therefore in the reconstruction a Gaussian approximation was made.

6.3.4.1 Reconstruction efficiency and fake track probability.

Reconstructed tracks are classified according to a hit quality factor, based on Monte Carlo information, and defined as the fraction of hits belonging to the track that were actually produced by the muon.

Fake tracks are defined as those with a hit quality factor lower than 10%. The fake track rate is then the average number of fake tracks per event.

Good tracks are those for which the hit quality factor exceeds 55%, and whose reconstructed momentum p_{rec} is sufficiently close to the true muon momentum p_{true} at the entrance of the muon spectrometer. For this purpose the cut $|\delta| < 4$ was applied to the momentum pull δ defined by:

$$\delta = \frac{(p_{rec} - p_{true}) / p_{true}}{\sigma_{th}}$$

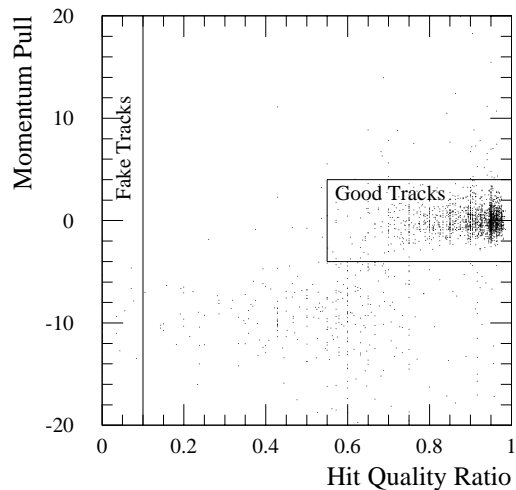


Figure 6-22 Momentum pull versus hit quality ratio (fraction of real muon hits used for the track reconstruction) for $p_T = 1 \text{ TeV}$.

Here σ_{th} is the resolution which would be theoretically expected for the generated track taking into account the momentum, direction and position of the muon at the entrance to the spectrometer. Figure 6-22 shows the regions for good and fake tracks in the plane of momentum pull versus hit quality ratio. The reconstruction efficiency is then defined as the fraction of events which contain a good track.

Figure 6-23 shows the dependence of the single muon reconstruction efficiency and the fake track probability on the transverse momentum p_T . As p_T increases, more secondary particles are produced by the muon. Hits from these secondaries can hide the muon hits and thus lead to wrong drift time measurements. They also create hits in tubes which are not traversed by the muon. The consequence is an increasing probability for reconstructing a fake track. In the same way the efficiency for finding good tracks decreases.

Figure 6-23 shows that the reconstruction efficiency does not change significantly if in the digitisation the MDT response description is improved from the old model (triangular markers) to the most realistic parametrisation (circular markers). Switching off the non-Gaussian tails in the tube resolution function has no impact at all (not displayed in the figure for reasons of visibility). The fake track probability, however, seems to depend on the MDT response (lower graphs in Figure 6-23). The more realistic and the more complex the description becomes, the less is the chance to build up a fake track from background hits. The details of this mechanism are not understood.

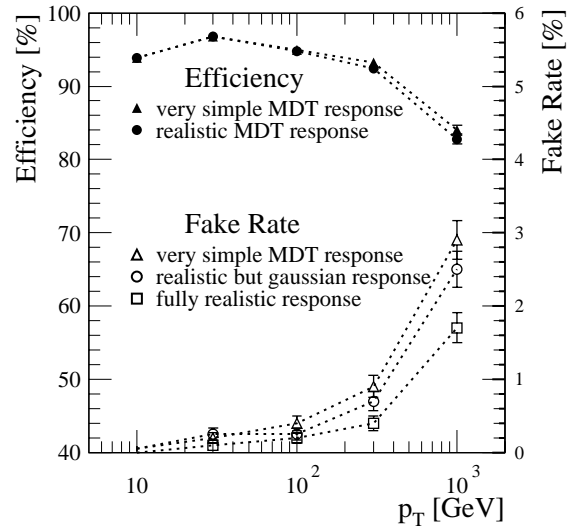


Figure 6-23 Reconstruction efficiency and fake track probability as a function of p_T for single muons.

6.4 Reconstruction of quasi-stable charged heavy particles

Heavy long lived particles are predicted in some extensions of the Standard Model. If these particles are charged and are not subject to a strong interaction, they behave as high mass muons. For masses of about 100 GeV, these particles travel at a speed significantly lower than that of light. Therefore they reach the Muon System with a time delay with respect to relativistic particles. For example, a particle with $\beta = 0.5$ reaches the Muon System with a 20 ns delay.

The aim of this study is to evaluate to what extent these particles can be reconstructed in the Muon System, and to estimate the β measurement accuracy. The combination of time and momentum measurement permits the evaluation of the particle mass [6-10]. The results of this study have been applied in Chapter 20 to the study of the supersymmetric partners of the τ lepton in models incorporating Gauge Mediated SUSY breaking (GMSB) [6-11]. In the following, $\tilde{\tau}$ indicates a heavy charged particle. A detailed description of this analysis can be found in [6-12].

6.4.1 Particle tracking and reconstruction

The study was performed for particles with a fixed mass of 101 GeV, as suggested by GMSB; the only relevant parameter is the β of the particle. Table 6-3 shows the list of the generated samples. Each sample consisted of 500 events. Particles at fixed p_T were simulated at $\eta = 0.1$ and $\phi = 2^0$. In addition, a reference sample of 500 GeV muons was generated in the same region as the signal samples.

Table 6-3 Generated samples.

Particle type	p (GeV)	Particle β	η, ϕ
$\tilde{\tau}$	50/76/135/200/500	~0.5, 0.6, 0.7, 0.8, 0.98	0.1, 2^0
muon	500	1.0	0.1, 2^0

All the simulated events were reconstructed accounting, in the pattern recognition program, for the time of flight through the detector. The χ^2 of the reconstructed track was studied as a function of β , determining the value where χ^2 is minimum. This analysis has shown that β can be estimated with an accuracy $\sigma(\beta)/\beta^2 \approx 0.03$; this is consistent with expectation from the muon detector time resolution of about 0.7 ns. The momentum resolution is found to be essentially the same as for muons of the same momentum, except at low energy where it is slightly worse [6-12].

6.4.2 Reconstructed mass

Combining the reconstructed momentum together with the reconstructed β , it is possible to estimate the particle mass. The mass resolution as a function of β and the mass distributions for the event samples are shown in Figures 6-24 and 6-25.

In conclusion, this analysis has shown that ATLAS can measure the mass of heavy stable leptons with an accuracy of 5% for values of β in the range 0.5 to 0.9 for a mass of about 100 GeV. A more detailed investigation needs knowledge of production cross-sections and spectra of the produced heavy particles, and this can only be done by assuming specific theoretical scenarios for the production of these particles.

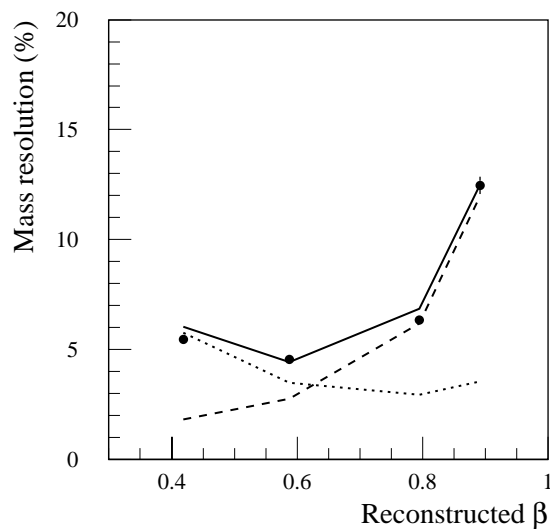


Figure 6-24 Mass resolution as a function of β for the heavy particle samples. The dashed line is the contribution from the β measurement error, the dotted line is the one from momentum.

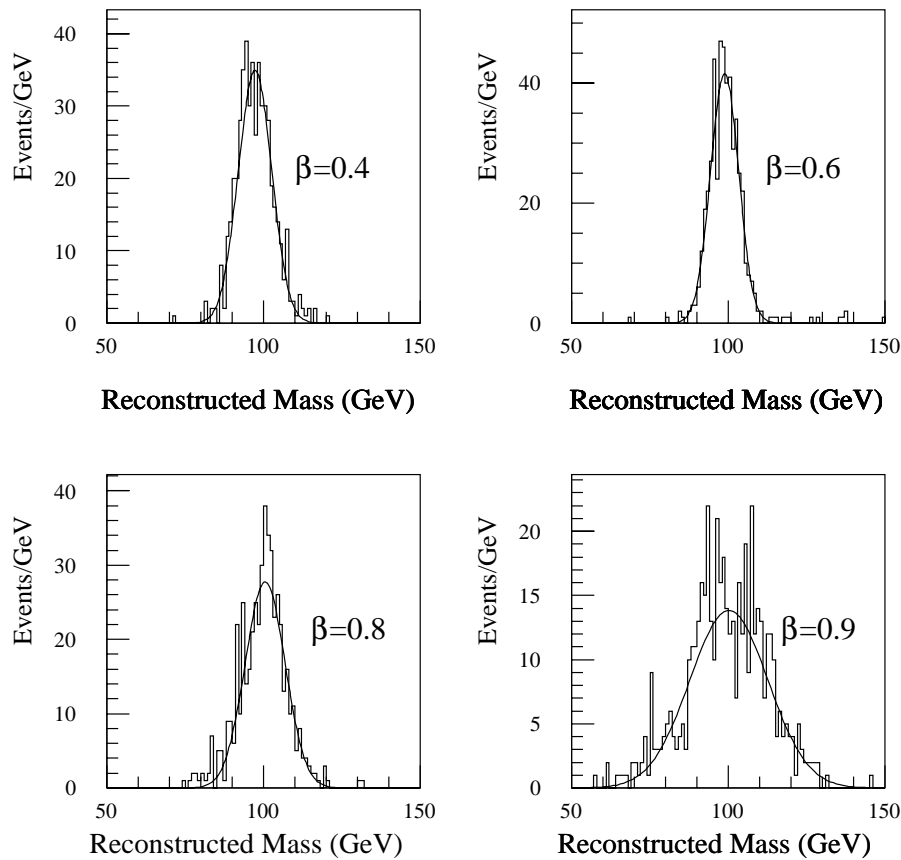


Figure 6-25 Reconstructed mass of the heavy particles with momenta of 50, 76, 135 and 200 GeV.

6.5 References

- 6-1 ATLAS collaboration, Muon Spectrometer Technical Design Report, CERN/LHCC/97-22 (1997).
- 6-2 ATLAS Collaboration, Technical Coordination Technical Design Report, CERN/LHCC/99-01 (1999).
- 6-3 R. von Boehn-Buchholz *et al.*, 'The conceptual design of the ATLAS EM Muon Chamber support structures', ATLAS Internal Note ATL-MUON-98-232 (1998).
- 6-4 A. Rimoldi, 'Geometrical Acceptance for the Trigger Chamber System and studies of the reaction $H \rightarrow ZZ^* \rightarrow 4\mu$ from the acceptance point of view', ATLAS Internal Note ATL-DAQ-98-119 (1998).
- 6-5 ATLAS collaboration, ATLAS LVL1 Technical Design Report, CERN/LHCC/98 (1998).
- 6-6 L. Chevalier *et al.*, 'Test of the magnetic field reconstruction procedure with a racetrack-coil prototype', ATLAS-COM-MUON NOTE-99-012 (1999).
- 6-7 L. Chevalier *et al.*, 'AMDB_SIMREC: A Structured data base Atlas internal for the ATLAS Spectrometer Simulation Program', ATLAS Internal Note ATL-MUON-97-148 (1997).
- 6-8 M. Deile *et al.*, 'MDT Track fitting with the Maximum Likelihood Method', ATLAS Internal Note ATL-MUON-98-240 (1998).

- 6-9 T. Sammer, Autocalibration von Driftrohrkammern für das ATLAS-Myonenspektrometer, Diplomarbeit, University of Munich, 1997.
- 6-10 A. Nisati, S. Petrarca and G. Salvini, Rev. of Mod. Phys. Lett. **A12** (1997) 2213.
- 6-11 I. Hinchliffe and F.E. Paige, 'Measurements in Gauge Mediated SUSY Breaking Models at the LHC', hep-ph/9812233.
- 6-12 G. Polesello and A. Rimoldi, 'Reconstruction of quasi-stable charged sleptons in the ATLAS Muon Spectrometer', ATLAS Internal Note ATL-COM-MUON-99-008 (1999).